Article

One-Pot, One-Step Synthesis of Drug-Loaded Magnetic Multimicelle Aggregates

Chang Soo Kim,[∇] Dmitry Nevozhay,[∇] Rebeca Romero Aburto,[∇] Ashok Pehere, Lan Pang, Rebecca Dillard, Ziqiu Wang, Clayton Smith, Kelsey Boitnott Mathieu, Marie Zhang, John D. Hazle, Robert C. Bast, Jr., and Konstantin Sokolov*

Read Online

ACCESS | Metrics & More | Article Recommendations | SI Supporting Information

ABSTRACT: Lipid-based formulations provide a nanotechnology platform that is widely used in a variety of biomedical applications because it has several advantageous properties including biocompatibility, reduced toxicity, relative ease of surface modifications, and the possibility for efficient loading of drugs, biologics, and nanoparticles. A combination of lipid-based formulations with magnetic nanoparticles such as iron oxide was shown to be highly advantageous in a growing number of applications including magnet-mediated drug delivery and image-guided therapy. Currently, lipid-based formulations are prepared by multistep protocols. Simplification of the current multistep procedures can lead to a number of important technological advantages including significantly decreased processing time, higher reaction yield, better product reproducibility, and improved quality. Here, we introduce a one-pot, single-step synthesis of drug-loaded magnetic multimicelle aggregates (MaMAs), which is based on controlled flow infusion of an iron oxide nanoparticle/lipid mixture into an aqueous drug solution under ultrasonication. Furthermore, we prepared molecular-targeted MaMAs by directional antibody conjugation through an Fc moiety using Cu-free click chemistry. Fluorescence imaging and quantification confirmed that antibody-conjugated MaMAs showed high cell-specific targeting that was enhanced by magnetic delivery.
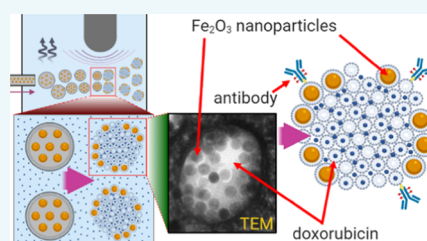
INTRODUCTION

Lipid-based nanoformulations, such as liposomes and micelles, collectively represent one of the most advanced and well-developed sets of technological platforms that are widely used to encapsulate and deliver various therapeutic and imaging agents in biological and biomedical research and clinical applications.[1−12] These formulations offer a number of attractive properties including biocompatibility, biodegradability, reduced toxicity, and capacity for size and surface modifications.[4] These features allowed early successful clinical applications of liposomal formulations for drug delivery such as liposome-encapsulated doxorubicin known as Doxil[13] and a number of other liposomal drugs that are already in clinical practice or are being evaluated in clinical trials.[14−17] Clinical adoption of lipid-based micelles is more limited so far; however, they were used in a number of preclinical studies as promising platforms for MRI contrast agents,[18−20] hydrophobic drugs,[21−24] and peptide[25] delivery.

Another clinically successful nanotechnology platform is based on superparamagnetic properties, most commonly, utilizing iron oxide nanoparticles (IONPs).[26] Clinically approved applications of IONPs include treatment of anemia,[27,28] contrast enhancement in MRI,[29] and hyperthermia therapy.[30,31] Furthermore, magnetic properties of IONPs have been used to achieve high contrast in magnetomotive optical,[32,33] ultrasound,[34] and photoacoustic imaging;[35]

to enhance the efficiency of site-specific delivery of magnetic nanoparticle-loaded stem cells;[36−38] and to provide spatial control over CRISPR-Cas9 genome editing.[39−41] In addition, detection of changes in the orientation of the magnetic moment of IONPs in an external magnetic field is a foundation for two emerging imaging and sensing modalities—magnetic particle imaging (MPI)[42,43] and magnetic relaxometry,[44] respectively.

Recognition of the strengths of these two platforms inspired development of hybrid approaches such as magnetic liposomes[45,46] or magnetic micelles.[47] Encapsulation of IONPs within lipid-based nanoformulations can enhance hydrophilicity, stability in plasma, better control of the pharmacological fate, and an overall improvement in their biocompatibility.[4] The initial application of magnetic lipid-based nanoformulations was to improve cell sorting using an external magnetic field.[45] Then, the range of applications was quickly extended to externally activated drug delivery by an alternating magnetic field (AMF),[48,49] magnet-mediated drug deliv-
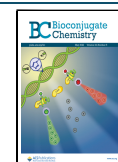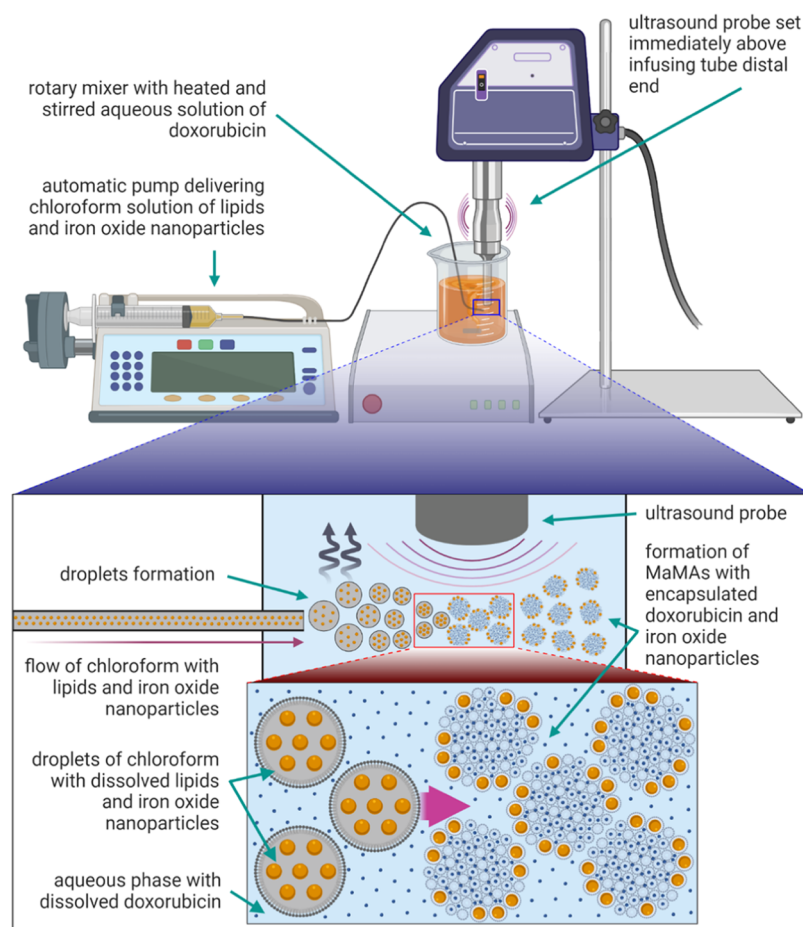
Figure 1. Schematic of a one-pot, one-step synthesis of drug-loaded magnetic lipid-based formulations. The laboratory setup (top) and an outline of the formation process. Magnetic multimicelle aggregates (MaMAs) were synthesized by controlled flow infusion of an IONPs/lipid mixture into an aqueous solution of doxorubicin under ultrasonication.

ery,[50−52] MRI contrast agents with improved imaging contrast and specificity,[47,53−56] image-guided drug delivery,[52] image-guided surgery,[57] image-guided immunotherapy,[58] and the list of possible applications continues to grow.[59]

Traditionally, lipid-based formulations are prepared by multistep processes that include formation of a thin lipid layer—"lipid cake", followed by a hydration step and finally extrusion that results in uniform unilamellar liposomes[60] or emulsification to produce micelles. For the synthesis of multifunctional lipid-based carriers, hydrophilic molecules or nanoparticles are, usually, added to the hydration solution and hydrophobic moieties are mixed with lipids in the "lipid cake". In the synthesis of magnetic lipid-based formulations, highly uniform superparamagnetic IONPs can be prepared by a common thermodecomposition reaction of an iron complex, i.e., $Fe(acac)_3$, that results in hydrophobic, oleic acid-coated nanoparticles. In this case, an extra step is required to stabilize magnetic nanoparticles in water suspension usually by applying an amphiphilic coating.[59,61] Simplification of the current multistep protocol for preparation of magnetic nanoformulations can lead to several important technological advantages including significantly decreased processing time, higher reaction yield, better product reproducibility, and improved quality. Therefore, it is highly desirable to develop a one-pot, one-step approach for the synthesis of multifunctional lipid-based formulations.

Here, we report a one-step synthesis of multifunctional magnetic lipid-based formulations using a simple fluidic infusion of a hydrophobic mixture of lipids and uniform oleic acid-coated magnetic nanoparticles (25 nm in core diameter) in chloroform into a hydrophilic drug-containing aqueous phase under ultrasonication (Figure 1). We optimized the flow speed, lipid-to-iron oxide nanoparticle ratio, and sonication power and showed that this approach results in reproducible, stable, and uniform multifunctional nanoparticles with encapsulated IONPs and a soluble anticancer drug—doxorubicin. Furthermore, we used functionalized lipids and Cu-free click chemistry for directional conjugation of HER2-targeted antibody, trastuzumab, to enable molecular-specific targeting of HER2 expressing breast cancer cells. Finally, the targeted multifunctional nanoparticles were used to treat breast cancer cells with and without an external magnetic field. Our results indicate that magnetic guidance significantly increases cancer cell death.

■ RESULTS AND DISCUSSION

Our approach to a one-pot, one-step synthesis of drug-loaded magnetic lipid-based formulations is based on controlled fluidic infusion of a mixture of oleic acid-coated IONPs and lipids in chloroform into a heated aqueous drug solution under a probe ultrasonicator (Figure 1). The rate of infusion was controlled by an automatic pump set at 35 mL/h. Our tests showed that increasing the speed of infusion beyond 35 mL/h
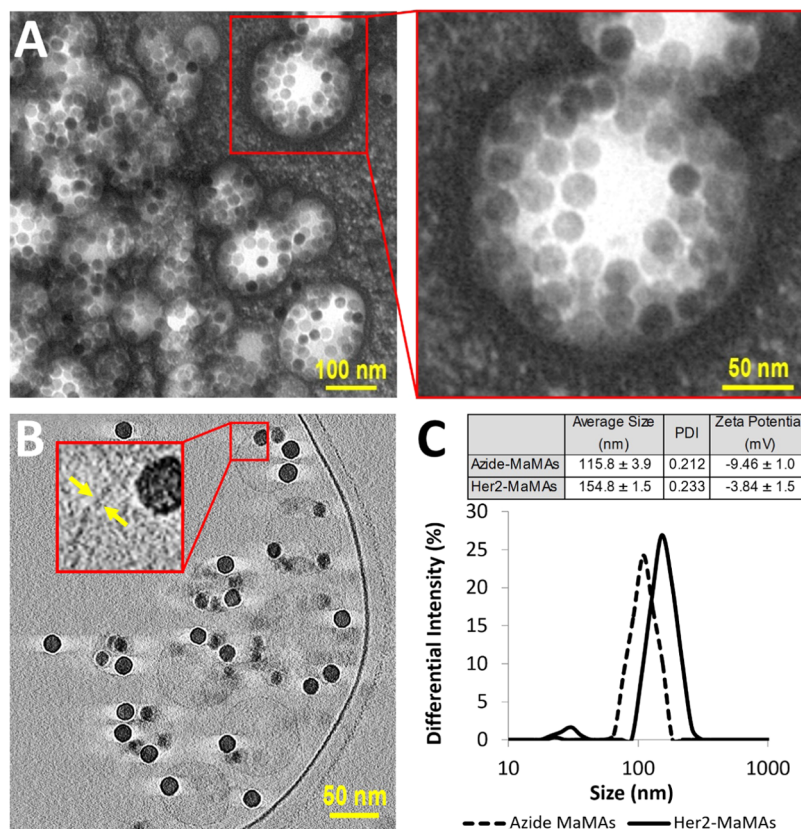
Figure 2. (A) TEM images of MaMAs obtained using negative staining with 2% uranyl acetate. (B) Cross-sectional cryo-EM images of MaMAs. Individual IONPs (25 nm in diameter) can be clearly seen within spherical structures. Note the absence of a visible lipid bilayer, indicating that these structures are not liposomes. (C) Size (DLS, intensity) and ζ-potentials of MaMAs before and after conjugation with trastuzumab.

resulted in the formation of larger structures and a decrease in their uniformity. The aqueous phase was heated to ∼80 °C to accelerate evaporation of chloroform. The probe sonicator tip with 6 mm diameter was placed at a distance of ∼2 mm from the end of the 0.76 mm inner diameter poly-ether-ether-ketone (PEEK) tube to quickly disperse the incoming lipid/nanoparticle mixture into small droplets. Then, chloroform evaporation and lipid self-assembly resulted in the formation of nanostructures with encapsulated IONPs (Figure 1).

TEM images of negatively stained samples revealed the presence of spherical structures with multiple ∼25 nm diameter IONPs inside (Figure 2A). To evaluate the morphology of these nanostructures, we carried out cryo-EM electron tomography (Figures 2B and S7 and Movies S1−S4). Cryo-EM did not show a lipid bilayer typical of a liposomal formulation, indicating that the observed structures are not liposomes. Further, IONPs are located along the periphery of the nanostructures without forming a continuous layer that rules out the possibility of hollow vesicles formed by the spherical self-assembly of nanoparticles coated with amphiphilic polymers that were described previously.[62] However, structures that are similar to the ones observed by us were previously reported in the case of hyperbranched conjugated polymers (HCPs) with 2 kDa poly(ethylene glycol) (PEG) arms[63−65] where PEGylated HCP micelles were shown to self-assemble into spherical multimicelle aggregates. Therefore, the cryo-EM data and analysis of the literature on various nanoformulations produced using amphiphilic polymers led us to the conclusion that our nanoparticles are consistent with MaMAs formed by a combination of IONPs and lipid micelles.

We used 26 cross-sectional images from cryo-EM reconstructed tomograms of individual MaMAs to estimate the number of IONPs per MaMA nanoparticle; the image stacks are shown in Movies S1−S4. We determined the median of six individual IONPs per MaMA with an interquartile range of 25−75% of 3−10 IONPs (Figure S7C).

Next, we acquired negatively stained TEM images using SerialEM montage mode with multiple overlapping fields of view (Figure S6) to evaluate the presence of a lipid coating around IONPs by determining whether they have a well-defined negatively stained coating layer, as was previously described.[66,67] The IONPs in the composite TEM image were classified into two groups: (I) nanoparticles either coated with a clearly visible negatively stained layer or residing within larger negatively stained areas with sizes significantly larger than individual IONPs and (II) isolated nanoparticles without a clearly visible lipid coating on their surface. The analysis showed that 8218 out of 8414 (97.7%) IONPs were clearly surrounded by a lipid coating and the remaining 196 (2.3%) IONPs did not have a clearly discernable negatively stained layer. These data indicate that the vast majority of IONPs are coated by a lipid layer and further indicate that most IONPs are associated with larger negatively stained structures, which we interpret as MaMAs according to the cryo-EM data.

Size analysis in suspensions of our particles by dynamic light scattering (DLS) showed the mean hydrodynamic diameter of ∼115 nm, polydispersity index (PDI) of 0.212, and ζ-potential of −9.46 mV (Figure 2C). In addition, we carried out size measurements using the nanoparticle tracking analysis (NTA) method, which directly images the Brownian motion of all

nanoparticles in a sample to derive their distribution. This approach has been successfully used for the characterization of various types of particles including PEGylated iron oxide nanoparticles with sizes less than 20 nm.[68] NTA showed a single dominant peak at ~133 nm, which contained ~90.84% of all MaMAs (Figure S4) that is in good agreement with DLS. A subpopulation of MaMAs around a minor peak at ~56 nm (3.74% of all particles, Figure S4) is consistent with the presence of isolated IONPs observed in TEM. Further, there was ~5.42% fraction with a size of ~243 nm. The combination of cryo-EM, negatively stained TEM, DLS, and NTA analyses indicates that our particles are predominantly spherical nanostructures with individual lipid-coated IONPs located on the periphery. These structures are consistent with previously reported multimicelle aggregates.[63−65] Since our nanoparticles contain magnetic IONPs, we refer to them as MaMAs.

For the synthesis of MaMAs, 1.97 mg of lipids and 0.4 mg of IONPs (based on the iron content measured by ICP-MS) were taken for a typical batch. The exact ratio of lipids is outlined in Table 1 and consisted of PEGylated DSPE phospholipids that

Table 1. Lipid Composition in a Typical Synthesis of Magnetic Lipid-Based Formulations

	lipid concentration (mg/mL)	mole fraction	volume (μL)	lipid mass (mg)
DSPE-PEG-1000	25	0.60	38.59	0.96
DSPE-PEG-2k-Azide	25	0.20	20.21	0.51
DSPE-PEG-2000	25	0.20	20.14	0.50
total		1.00	78.94	1.97

are commonly used in various biomedical applications[69−72] including clinical lipid formulations.[73−75] Specifically, 1,2-distearoyl-*sn*-glycero-3-phosphoethanolamine-N-[amino-(polyethylene glycol)-1000] (DSPE-PEG-1000), 1,2-distearoyl-*sn*-glycero-3-phosphoethanolamine-N-[amino(polyethylene glycol)-2000] (DSPE-PEG-2000), and 1,2-distearoyl-*sn*-glycero-3-phosphoethanolamine-N-[azido(polyethylene glycol)-2000] (DSPE-PEG-2k-Azide) were mixed at the molar ratios of 60%:20%:20%, respectively.

Ultrasonication power was varied from 20 to 40% of the maximum level of the ultrasonic probe tip sonicator (Cole−Parmer) to determine optimum conditions for the formation of monodispersed MaMAs with the smallest size. A relatively low power—20% of the maximum—resulted in a bimodal distribution with sizes of ~80 and ~234 nm (Figure S1). The ultrasonication power at 30% produced homogeneous MaMAs with sizes of ~118 nm, and increasing the power to 40% led to a relatively large size of ~277 nm. Therefore, the 30% power

setting was used throughout our studies. This experiment indicates the existence of a sweet spot for the ultrasonication power that might need to be readjusted if a different instrument or a probe tip size is used.

Next, the ratio of lipids to IONPs in the infusion chloroform mixture was optimized by changing the concentration of the nanoparticles from 0.1 to 1.6 mg/mL (Figure S2) while keeping the amount of the lipids the same (1.97 mg, Table 1). The size of MaMAs stayed the same at ~118 nm up to 0.4 mg/mL iron oxide concentration and it increased at higher concentrations (Figure S2). Therefore, we settled on the 0.4 mg/mL iron oxide concentration for the synthesis of MaMAs. The same relative amount of iron oxide and lipids was used throughout the study. We also evaluated the relative amounts of iron oxide and lipids retained in the preparations at the completion of the synthesis using ICP-MS and UV−Vis spectrophotometry for iron oxide and fluorescently labeled lipids for lipid quantitation. A typical batch retained ~81.7% of the iron oxide and ~69.8% of lipids at the completion of the synthesis relative to the initial total quantities.

The stability of MaMAs was studied in buffer solutions under different pH values: MES buffer at pH 6.5 and PBS at pH 7.4 at 4 °C, as well as in the presence of 10% and 100% FBS at 4 and 37 °C, pH 7.4, over periods of 6, 12, 24, and 48 h. The exposure to FBS at 37 °C was used to mimic a biological environment. After incubation under different conditions, the size of MaMAs was measured by DLS to assess stability (Figure S3). There were no substantial size changes and no evidence of nanoparticle aggregation even after exposure to 100% FBS confirming the stability of the MaMAs. We also measured the stability of MaMAs during 8 weeks of storage in 40 mM HEPES, pH 7.5, at 4 °C and found that their size measured by DLS decreased by ~8 nm while maintaining a good monodispersity with the PDI 0.158.

Trastuzumab antibodies were conjugated to azide-functionalized lipids on the surface of MaMAs by copper-free click chemistry (Figure 3). Click chemistry provides an attractive approach for functionalization of nanoparticles because it has sufficiently rapid reaction kinetics, a high selectivity, and bond stability.[77−82] We used a directional antibody conjugation strategy previously developed by us, where the carbohydrate moiety on the Fc portion of the trastuzumab antibody was first mildly oxidized with sodium periodate to produce aldehyde groups.[76] Then, the aldehyde groups were reacted with the aminooxy group of the bifunctional dibenzocyclooctyne (DBCO)-PEG-aminooxy linker. The linker−antibody conjugates were then attached to MaMAs through the click reaction between DBCO and azide groups, resulting in HER2-targeted MaMAs (aHER2-MaMAs). The enzyme-linked
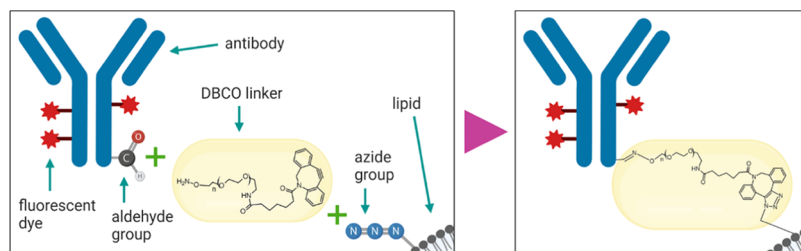

Figure 3. Schematic of fluorescently labeled trastuzumab antibody conjugation to azide-functionalized MaMAs through the bifunctional DBCO-PEG-aminooxy linker using Cu-free click chemistry. This approach utilizes mild oxidation of a carbohydrate moiety on the antibody's Fc portion to form aldehyde groups.[76]
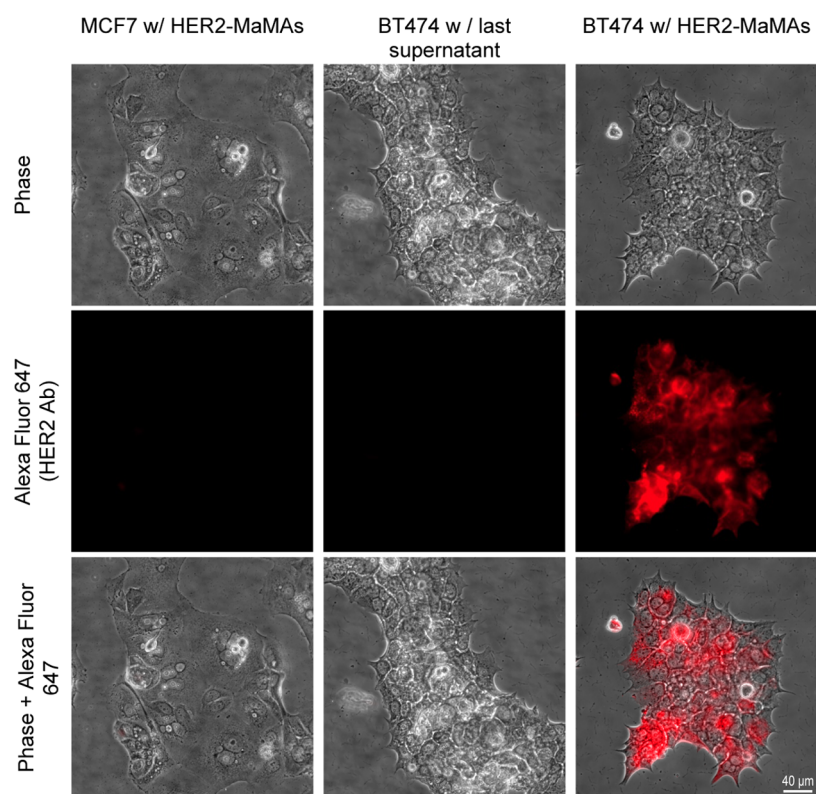
Figure 4. Optical microscopy images of (from left to right) HER2⁻ MCF7 cells after incubation with A647-aHER2-MaMAs; HER2⁺ BT474 incubated with the supernatant collected after the last washing step following synthesis of A647-aHER2-MaMAs (a control for free residual Alexa Fluor 647-labeled trastuzumab antibodies); and HER2⁺ BT474 cells after incubation with A647-aHER2-MaMAs. Note the lack of a fluorescence signal from HER2⁺ BT474 cells incubated with the supernatant; this indicates that the fluorescence after incubation with A647-aHER2-MaMAs is associated with the nanoparticles rather than with residual free antibodies. The images were acquired using a Zeiss Axio Observer.Z1m microscope equipped with a Hamamatsu ORCA-ER camera (Bridgewater, NJ) under a 40× objective lens. Fluorescence images were obtained with BP 640/30 nm excitation and BP 690/50 nm emission filters. Scale bar is 40 μm.

immunosorbent assay (ELISA) was used to determine the antibody/aHer2-MaMA ratio. Specifically, this ratio was calculated in terms of the number of antibody molecules per iron oxide nanoparticle. The amount of encapsulated IONPs per MaMA was determined by inductively coupled plasma mass spectrometry (ICP-MS). The combination of ELISA and ICP-MS showed that there was ~1 antibody/iron oxide nanoparticle in a typical batch of aHER-MaMAs. The antibody−MaMA conjugates had a hydrodynamic diameter of ~155 nm, PDI of 0.233, and a surface charge of −3.84 mV, which was more neutral than the one for unconjugated MaMAs (Figure 2C).

Targeted MaMAs were conjugated with Alexa Fluor 647-labeled trastuzumab (A647-aHER-MaMAs) to evaluate their molecular specificity in HER2⁺ positive BT474 and HER2⁻ negative MCF7 breast cancer cells. Fluorescence microscopic images (Figure 4) showed a strong fluorescent Alexa Fluor 647 signal from HER2⁺ BT474 and no fluorescence from HER2⁻ MCF7 after labeling with A647-aHER2-MaMAs, indicating the molecular specificity of the targeted MaMAs. To ensure that the observed fluorescence was not associated with residual free Alexa Fluor 647-labeled antibodies left after washing of targeted MaMAs, we incubated HER2⁺ BT474 cells with the last supernatant collected during centrifugal purification of A647-aHER2-MaMAs (Figure 4); no fluorescence signal was observed in this case, confirming that the fluorescence in HER2⁺ BT474 cells labeled with A647-aHER-MaMAs was due to the targeted MaMAs. To further demonstrate molecular-

specific labeling with aHER-MaMAs, we carried out a blocking assay where HER2⁺ BT474 were preincubated with free trastuzumab antibodies before labeling with A647-aHER-MaMAs (Figure 5). The cells did not exhibit any significant Alexa Fluor 647 signal indicating that A647-aHER2-MaMAs did not interact with cells after binding sites on HER2 receptors were blocked by free antibodies (Figure 5B,C).

After establishing the molecular specificity of aHER2-MaMAs, we carried out initial evaluation of their performance in molecular-specific and magnet-mediated drug delivery in cell cultures. Doxorubicin was used as a model water-soluble drug for MaMA loading. Drug-loaded MaMAs were synthesized using the single-step reaction, shown in Figure 1, with doxorubicin added to the aqueous phase. Then, the MaMAs were conjugated with unlabeled trastuzumab antibodies (Figure 3). The hydrodynamic diameter of drug-loaded MaMAs changed from ~124 to ~144 nm after antibody attachment, which was consistent with the size changes observed for MaMAs without a drug (Figure 2C). To visualize cellular uptake of targeted doxorubicin-loaded MaMAs (aHER2-DOX-MaMAs), HER2⁺ BT474 and HER2⁻ MCF7 cells were grown in imaging chambers and were incubated with the MaMAs for 2 h at 37 °C either with or without a permanent 1 cm neodymium magnet placed under the chambers. Then, the excess of aHER2-DOX-MaMAs was removed, and the cells were fixed in 4% paraformaldehyde and imaged under an optical microscope (Figure 6).
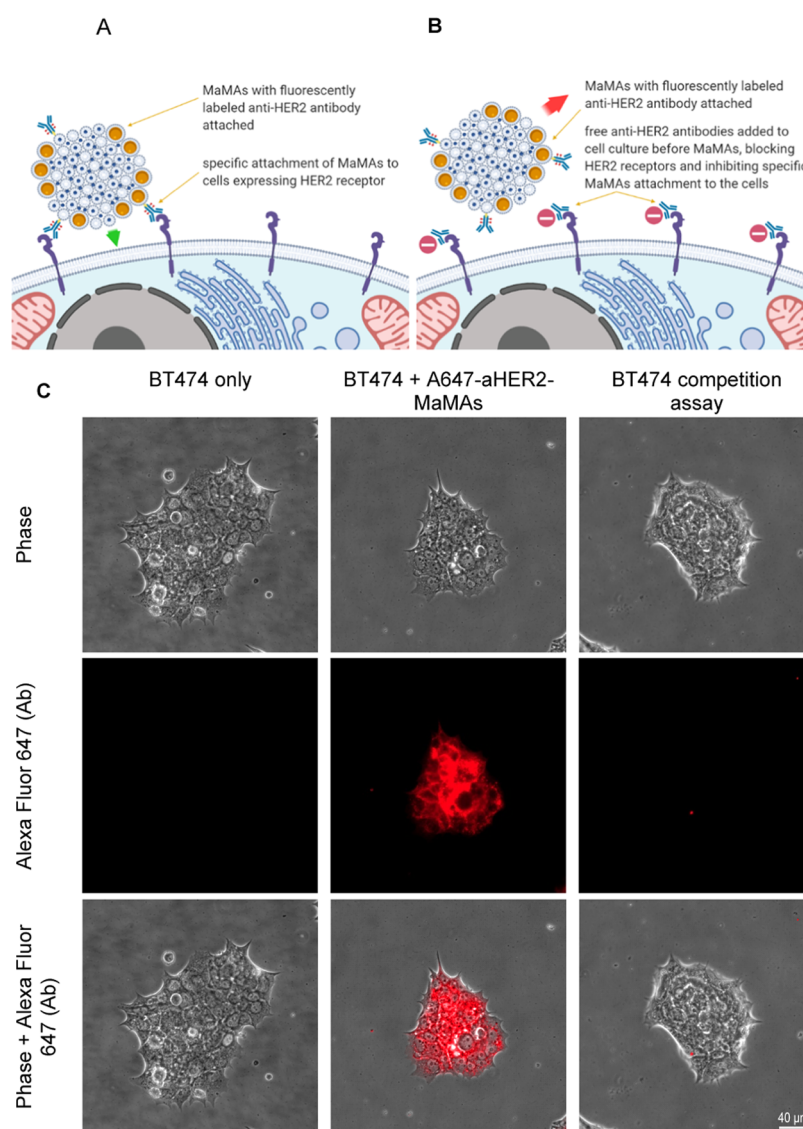
Figure 5. Blocking assay with HER2⁺ BT474 cells. Schematic of the study: (A) targeted MaMAs conjugated with fluorescently labeled trastuzumab antibodies (A647-aHER2-MaMAs) binding to HER2 positive cells; (B) blocking assay in which HER2 receptors are blocked by preincubation with free trastuzumab that precludes subsequent binding of A647-aHER2-MaMAs. (C) Optical microscopy images of (from left to right) BT474 cells alone (untreated control); BT474 A647-aHER2-MaMAs (BT474 cells labeled with A647-aHER2-MaMAs); and BT474 blocking assay where BT474 cells were preincubated with free trastuzumab antibodies before labeling with A467-aHER2-MaMAs. The images were acquired using a Zeiss Axio Observer.Z1m microscope equipped with a Hamamatsu ORCA-ER camera (Bridgewater, NJ) under a 40× objective lens. Fluorescence images were obtained with BP 640/30 nm excitation and BP 690/50 nm emission bandpass filters. Scale bar is 40 μm.

Fluorescence images show a strong doxorubicin fluorescence signal from BT474 cells with or without a magnet and from MCF7 cells in the presence of a magnet (Figure 6). No doxorubicin fluorescence was detectable from MCF7 cells without a magnet. These data indicate that both the molecular targeting and the magnetic force can effectively drive the delivery of doxorubicin encapsulated in aHER2-DOX-MaMAs to cancer cells.

To evaluate the cytotoxic effect of aHER2-DOX-MaMAs, we carried out a proliferative cell assay. First, we established the sensitivity of both BT474 and MCF7 cells to treatment with free doxorubicin. Both cell lines were incubated with various concentrations of doxorubicin for 72 h, and then the antiproliferative effect of the treatment was assessed using the AlamarBlue viability dye (Figure 7A) in comparison with untreated cells. The cells were sensitive to doxorubicin

treatment in a dose-dependent manner. Based on the treatment curves, we chose 0.35 μg/mL as the initial doxorubicin concentration for cell incubation with aHER2-DOX-MaMAs. The cells were incubated with the drug-loaded nanoparticles either with or without a magnet for 72 h. The surviving fractions of BT474 and MCF7 cells after 72 h of incubation with aHER2-DOX-MaMAs at the 0.35 μg/mL doxorubicin concentration were 49.1 ± 7.8% and 72.6 ± 7.4%, respectively, which are comparable to the effect of the free drug at the same equivalent concentration (Figure 7B). Further, incubation with a magnet did not have any statistically significant improvement of the aHER2-DOX-MaMAs inhibitory effect on cell proliferation in both cell lines (Figure 7B).

We hypothesized that the similar antiproliferative effect of the free drug and the drug-loaded nanoparticles was due to the long continuous incubation time and a relatively high drug
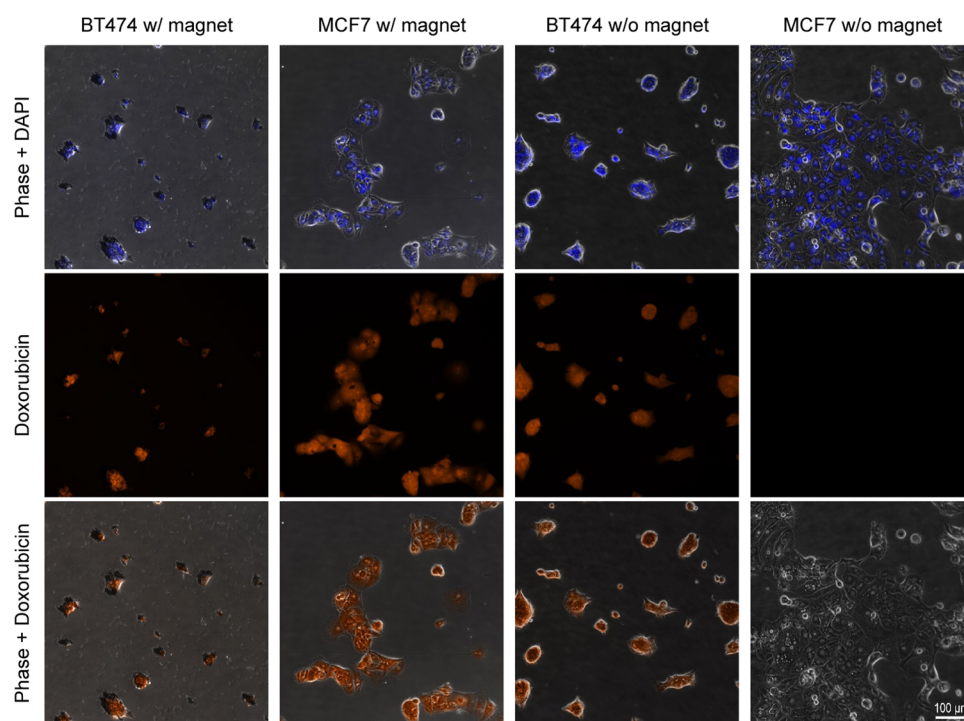
Figure 6. HER2$^+$ BT474 and HER2$^-$ MCF7 cells after incubation with aHER2-DOX-MaMAs at 37 °C with or without a permanent magnet: (top row) combined phase and DAPI images; (middle row) fluorescence images of doxorubicin; and (bottom row) combined phase and doxorubicin images. The images were acquired using a Zeiss Axio Observer.Z1m microscope equipped with a Hamamatsu ORCA-ER camera (Bridgewater, NJ) under a 40× objective lens. Fluorescence images were obtained with BP 550/25 nm excitation and BP 605/70 nm emission filters for doxorubicin detection and G 365 nm excitation, BP 445/50 emission filters for DAPI. Scale bar is 100 μm for all images.
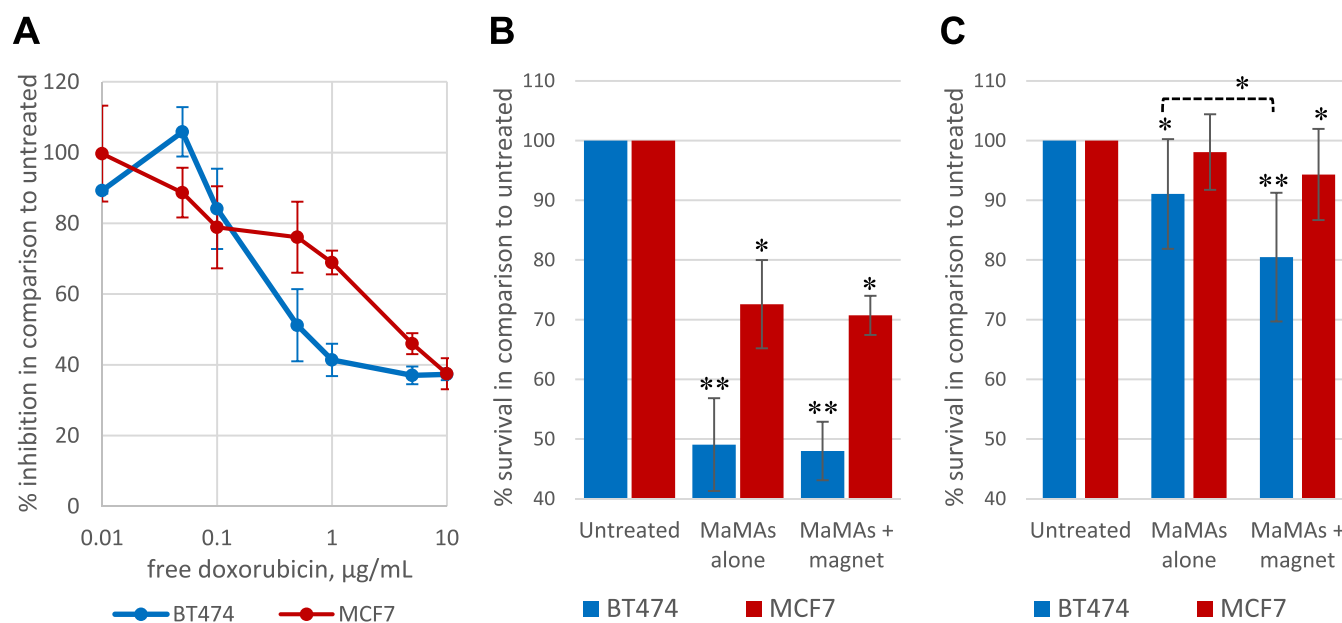

Figure 7. Antiproliferative effect in BT474 and MCF7 cells produced: (A) by free doxorubicin after continuous incubation with various drug concentrations for 72 h ($n = 3$); (B) after 72 h of continuous incubation with aHER2-DOX-MaMAs at 0.35 μg/mL free doxorubicin equivalent concentration ($n = 3$); (C) after 2.5 h of total incubation with aHER2-DOX-MaMAs at 0.0875 μg/mL free doxorubicin equivalent concentration ($n = 11$); in panel (C) a magnet was applied only during the first 30 min of incubation with the aHER2-DOX-MaMAs.

concentration that resulted in a high doxorubicin uptake by cells under all conditions (i.e., regardless of the active targeting or magnetic enhancement afforded by the nanoparticles). Therefore, we modified the assay to more closely resemble drug delivery *in vivo* where the availability of magnetically sensitive drug carriers would be limited by their blood

circulation time. To this end, we decreased the total incubation time with aHER2-DOX-MaMAs to 2.5 h, which is similar to the reported half-life time in blood circulation during an initial phase of systemic delivery of liposomal doxorubicin formulations.[73,83,84] Further, we decreased the concentration of aHER2-DOX-MaMAs 4 times to the equivalent of 0.0875

μg/mL of free doxorubicin. Magnets were applied only during the first 30 min of the incubation, which resulted in clearly visible nanoparticle sedimentation to the bottom of the wells where the magnetic field was applied, thus increasing the local concentration of aHER2-DOX-MaMAs at the surface of the wells right next to the growing cells. After completion of the full 2.5 h of incubation, media containing aHER2-DOX-MaMAs was removed and was replaced with the fresh one, followed by an additional 72 h of incubation and proliferation assessment (Figure 7C). Under the significantly shorter drug carrier incubation time, the application of a magnetic field had an additive antiproliferative effect of ~10% in the case of HER2$^+$ BT474 cells ($p < 0.01$). Further, HER2$^-$ MCF7 cells incubated with the combination of aHER2-DOX-MaMAs and a magnet showed a relatively small (~6%) but statistically significant inhibition of proliferation in comparison to untreated cells ($p < 0.05$), while no statistically significant inhibition was observed in the absence of a magnet. These data demonstrate that an external magnetic field can improve outcomes of cancer cell treatment with drug-loaded MaMAs when there are time constraints on drug delivery (e.g., blood circulation time).

CONCLUSIONS

Here, we synthesized novel drug-loaded magnetic lipid-based formulations MaMAs using a single-step, one-pot synthesis with ultrasonication. After optimizing the synthesis, we conjugated the anti-HER2 antibody (trastuzumab) to the surface of MaMAs through an Fc antibody moiety using Cu-free click chemistry. Fluorescence imaging showed that antibody-conjugated MaMAs had a high specificity for HER2-positive cancer cells. Further, we demonstrated that application of an external magnetic field can significantly enhance the antiproliferative activity of doxorubicin-loaded HER2-targeted MaMAs in the treatment of HER$^+$ breast cancer cells. Taken together, these data demonstrate that our synthesis can be used for efficient production of drug-loaded molecular-targeted MaMAs for drug delivery applications.

METHODS

Materials. The oleic acid-coated IONPs with a diameter of 25 nm (3.2−4 mg/mL) were provided by Imagion Biosystems. The dibenzocyclooctyne (DBCO)-PEG-aminooxy linker (3400 Da) was purchased from Nanocs. Lipids 1,2-distearoyl-*sn*-glycero-3-phosphoethanolamine-N-[amino-(polyethylene glycol)-1000] (DSPE-PEG-1000), 1,2-distearoyl-*sn*-glycero-3-phosphoethanolamine-N-[amino(polyethylene glycol)-2000] (DSPE-PEG-2000), 1,2-distearoyl-*sn*-glycero-3-phosphoethanolamine-N-[azido(polyethylene glycol)-2000] (DSPE-PEG-2k-Azide), and 1,2-distearoyl-*sn*-glycero-3-phosphoethanolamine-N-[amino(polyethylene glycol)-2000]-N-(Cyanine 5) (DSPE-PEG-2000-Cy5) were from Avanti Polar Lipids, Inc. Doxorubicin was from Pfizer, trastuzumab as a lyophilized sterile powder (supplied in a vial containing 150 mg) was from Genentech, chloroform was from Sigma, and silicone oil was from Merck.

Synthesis of MaMAs with and without Doxorubicin. For the synthesis of MaMAs, 1.97 mg of lipids and 0.4 mg of iron (based on the iron content measured using ICP-MS) were used for a typical batch. For the synthesis of larger batches of MaMAs, the volume of this chloroform mixture was increased while concentrations of all components were kept the same. A detailed composition of lipids is shown in Table 1. In a typical synthesis, 50 mL of deionized water in a glass beaker was heated to the temperature of 80 °C on a Super-Nuova Multi-Place hotplate (Thermo Scientific) with magnetic stirring, and doxorubicin was added to the aqueous phase; note that 0.2 mg was used in microscopy experiments and 10 mg in cell proliferation assay experiments. Synthesis of doxorubicin-free MaMAs was carried out following the same protocol but without the drug in the aqueous phase. Lipids (all in chloroform solutions) and oleic acid-coated IONPs (also in chloroform) were mixed and the total volume was brought to 1 mL by adding additional chloroform. The mixture was drawn into a 1 mL (a 10 mL syringe was used for larger batches) gastight syringe (Hamilton) connected to a flexible poly-ether-ether-ketone (PEEK) tube with 0.76 mm inner diameter (IDEX Health & Science) using an epoxy gel (Devcon). The distal end of the tube was placed inside the water in the beaker, and a 6 mm diameter ultrasonic probe (Cole-Parmer threaded ultrasonic probe) was placed just above the tube's distal end under water. The ultrasound probe sonicator (CPX 500, Cole-Parmer) was set to the 30% power output, and the lipid/nanoparticle chloroform mixture was infused into the pre-heated water phase under ultrasonication at the 35 mL/h flow rate that was controlled using a KDS-210 automatic syringe pump (KD Scientific). The entire water phase with MaMAs solution from the beaker was collected and centrifuged at 3100g for 40 min and 10 °C to sediment larger aggregates. The supernatant was transferred to 15 mL 10 kDa MWCO Amicon filter tubes (Millipore Sigma) and centrifuged for 18 min at 3100g and 10 °C to concentrate MaMAs solution. The collected solution (ca. 200 μL) on the filter was transferred to 1.5 mL microcentrifuge tubes and centrifuged for 30 min at 16 900g at 10 °C. The supernatant was discarded carefully by pipetting it out, and the precipitate containing MaMAs was resuspended in 1 mL of 40 mM HEPES, pH 7.5. The last washing step in microcentrifuge tubes was repeated two more times (total three washings), and the final precipitate of MaMAs was resuspended in 1 mL of 40 mM HEPES, pH 7.5.

The size and surface charge of MaMAs were measured with a particle size and z-potential analyzer using dynamic light scattering (DelsaNano, Beckman Coulter). Size distribution reconstruction was acquired using the NNLS algorithm. Each size measurement was done using 300 acquisitions and 3 repetitions to ensure reproducibility. Additional size measurements were carried out using the nanoparticle tracking analysis method (Nanosight NS300, Malvern Panalytical). The concentration of IONPs in preparations of MaMAs was determined by the iron content using inductively coupled plasma mass spectrometry (ICP-MS). In addition, we created a calibration curve between ICP-MS results and the UV absorbance of MaMAs at 370 nm following a previously published protocol.[85] Then, the calibration curve was used to determine the concentration of iron content in MaMAs. The overall number of iron nanoparticles in the suspension of MaMAs and their concentration were estimated from the iron content using the iron oxide density and known size of iron nanoparticles (25 nm). This was later used as a surrogate metric to estimate molarity for the conjugation reaction between antibodies and MaMAs (see below). The doxorubicin concentration in MaMAs was estimated by measuring its fluorescence at 470/560 nm excitation and emission,[86] respectively, using a Synergy H1 fluorometer/plate reader (Biotek). Solutions with known doxorubicin concentrations

were used to create a calibration curve using linear regression. Then, the concentration of doxorubicin in MaMAs was calculated using their background-corrected fluorescence values and the formula from the linear regression fit of the standard curve.

Determination of the Amount of Lipids in the Final Preparation. We used the same protocol for the preparation of MaMAs as described above, with the exception that a portion of DSPE-PEG-2000 (12%) was replaced with the same molar amount of the DSPE-PEG-2000-Cy5 lipid containing the Cyanine 5 fluorescent dye. We collected all supernatants during centrifugal washing steps. Then, all collected supernatants and the final MaMAs were lyophilized and resuspended in chloroform, and their fluorescence was measured at 645 nm excitation and 665 nm emission using a Synergy H1 plate reader (Biotek). A standard curve was built using linear regression fitted fluorescence values of known concentrations of the DSPE-PEG2000-Cy5 lipid in chloroform. The concentration of the DSPE-PEG2000-Cy5 lipid in the collected supernatants and the MaMA's sample were calculated using their fluorescence values and formula from the regression fit of the standard fluorescence curve. Then, the relative amount of lipids in all supernatants and the MaMA's sample was calculated using the determined concentrations and the known total volumes of the samples.

Transmission Electron Microscopy. An aliquot (10 μL) of MaMAs was placed on 100 mesh carbon-coated, Formvar-coated copper grids pretreated with poly-L-lysine for ~1 h. For imaging with negative staining, the samples were negatively stained with Millipore-filtered aqueous 2% uranyl acetate. The stain was blotted dry from the grids with a filter paper, and the samples were allowed to dry. Then, the samples with or without negative staining were examined in a JEM 1010 transmission electron microscope (JEOL USA, Inc., Peabody, MA) at an accelerating voltage of 80 kV. Digital images were obtained using an AMT imaging system (Advanced Microscopy Techniques Corp., Danvers, MA).

Cryo-Electron Tomography. The preparations were diluted to 2×10^{12} MaMAs/mL concentrations with HEPES buffer. Then, 3 μL of each sample was applied to a Quantifoil R 1.2/1.3 Cu 200 mesh grid or a Lacey Carbon 300 Cu mesh grid that had been glow-discharged for 5 s using a PELCO easiGlow system (Ted Pella, Inc.) at 15 mA and 0.3 mBar. Grids were then plunge-frozen in liquid ethane with a Vitrobot Mk IV (Thermo Fisher Scientific) operated at 4 °C and 100% humidity, with a blot time of 2 s and wait time of 5 s. The grids were stored in liquid nitrogen until imaging. Cryo-electron tomography was performed on a Titan Krios TEM operated at 300 kV and equipped with a Gatan K2 camera (Gatan, Inc., Pleasanton, CA). Tilt series were collected using SerialEM at a nominal magnification of 14 000× (pixel size of 1.72 Å/pixel) with a tilt range of ±60 and 3° increment. Each projection was collected as a dose-fractioned movie of 10 frames with an exposure time of 0.65 s and a dose of 2.19 e$^-$/Å2. Alignment and reconstruction were performed in IMOD software.[87]

Antibody Conjugation to MaMAs. Conjugation was carried out using copper-free click chemistry with a 100:1 molar ratio of antibodies to iron nanoparticles with the latter being used as a surrogate estimation of MaMAs' concentration. After estimation of the iron content and number of iron nanoparticles in MaMA batches using ICP-MS/UV−Vis as described in the MaMA synthesis section, an appropriate amount of the antibody was estimated for each batch

individually. In a typical reaction, for each 1 mg of iron, 0.364 mg of the trastuzumab antibody was used.

The trastuzumab antibody was conjugated with the dibenzocyclooctyne (DBCO)-PEG-aminooxy linker (Nanocs) as follows. A required amount of antibody (typically 0.364 mg) was added to 3 mL of 1:1 v/v mixed solution of 100 mM Na$_2$HPO$_4$ and 100 mM NaH$_2$PO$_4$ and transferred to an Amicon 10 kDa MWCO centrifugal filter tube. The solution was centrifuged for 18 min at 3100g and 10 °C. Solution of the antibody remaining on top of the filter was recovered (typically ~90 μL), mixed with 10 μL of 100 mM solution of sodium periodate, and incubated in a 1.5 mL microcentrifuge tube on ice for 30 min at 250 rpm on a rotary shaker in the dark. After that, 500 μL of PBS (Ca/Mg free) was added to the solution to quench the oxidation and incubated for 5 more min in the same conditions. Then, the solution was transferred to an Amicon 10 kDa MWCO filter tube, and an additional 3 mL of PBS (Ca/Mg free) was added to the mixture, followed by centrifugation for 18 min at 3100g and 10 °C. Typically, ~70 to 100 μL of solution from the top of the filter was mixed with 600 μL of PBS (Ca/Mg free) and centrifuged again in the same 10 kDa MWCO filter tube two more times to wash the antibody from sodium periodate. The washed antibody was reconstituted in 600 μL of PBS (Ca/Mg free). Then, 2 μL of 49 mM solution of the dibenzocyclooctyne (DBCO)-PEG-aminooxy linker (3400 Da, Nanocs) in DMSO was added per each 0.1 mg of the antibody. The mixture was incubated at room temperature on a rotary shaker at 250 rpm for 1 h and transferred to an Amicon 100 kDa MWCO filter tube. The linker−antibody conjugates were washed three times in a centrifuge filter tube at 14 000g for 10 min at 10 °C. The first two rounds of washing were done in PBS (Ca/Mg free) and the last one was done in 40 mM HEPES, pH 7.5, to exchange the buffer for the next step. Typically ~70 to 300 μL of final washed antibody−linker solution in 40 mM HEPES, pH 7.5 was recovered for subsequent conjugation to MaMAs. To synthesize MaMAs with fluorescently labeled antibodies, the antibody molecules were labeled with the Alexa Fluor 647 dye (Invitrogen) according to the manufacturer's protocol prior to the attachment of the linker.

Appropriate amounts of MaMAs (typically 1 mg of iron content) and antibody−linker conjugates from the previous step (typically 0.364 mg of total mass) were mixed together in 40 mM HEPES, pH 7.5, and the total volume of the mixture was brought to 1 mL using 40 mM HEPES, pH 7.5. The suspension was incubated overnight at 4 °C. The MaMAs with attached antibodies were washed by centrifugation three times in 40 mM HEPES, pH 7.5 at 6200g for 30 min at 10 °C. After the third wash, the antibody-conjugated MaMAs were collected by placing microcentrifuge tubes inside a Dyna-Mag-2 magnetic separation device (Thermo Fisher Scientific) and leaving it overnight at 4 °C. The supernatant was discarded, and washed MaMAs were resuspended in 0.3 mL of 40 mM HEPES, pH 7.5.

ELISA for the Antibody Content of MaMAs. To create the standard curve, the raw ELISA data for different concentrations of trastuzumab antibody−linker solution was fit to a four-parameter logistic regression model: $y = d + \frac{a - d}{1 + \left(\frac{x}{c}\right)^b}$, where "$y$" are the ELISA readings and "x" are the antibody concentrations measured by UV−Vis spectrophotometry. The ELISA readings measured for different dilutions of the antibody-conjugated MaMAs solution were

then fit to the standard curve to determine the antibody concentration of the nanoparticle solution. To calculate the average ratio of antibodies conjugated per iron oxide nanoparticle, the antibody concentration was divided by the concentration of IONPs, determined from ICP-MS measurements of the iron concentration.

Cell Imaging. BT474 (HER2 positive) and MCF7 (HER2 negative) cells with 50 000 cells/well in 10% FBS containing DMEM media were seeded in 4-well imaging glass slides (Nunc Lab-Tek II Chamber Slide System, Thermo Fisher Scientific) and incubated overnight before imaging studies. MaMAs conjugated with Alexa Fluor 647-labeled antibodies were added to each chamber at the concentration of 5 μg of iron oxide, and the cells were incubated with the nanoparticles overnight at 37 °C in 5% CO_2. For the blocking assay, 5 μg of the free trastuzumab antibody was added to each chamber for 2 h before addition of the fluorescently labeled trastuzumab-conjugated MaMAs, followed by overnight incubation at 37 °C in 5% CO_2. After incubation, the cells were washed three times with PBS buffer and fixed with 4% paraformaldehyde for 30 min at room temperature and, then, imaged using a Zeiss Axio Observer Z1m microscope (Zeiss) equipped with a Hamamatsu ORCA-ER camera (Bridgewater, NJ).

Cell Proliferation Assay. BT474 and MCF7 cells were seeded at 5,000 cells/well density in 96-well plates containing 200 μL of DMEM media supplemented with 10% FBS and incubated at 37 °C and 5% CO_2 for the whole duration of experiments. Cells were incubated overnight before applying any treatments to allow for cells' attachment to the plates. Free doxorubicin was added to treated wells at various concentrations, and cells were incubated for 72 h before a proliferation assay with AlamarBlue[88] (Invitrogen). AlamarBlue is a viability assay based on the nonfluorescent, nontoxic, and cell-permeable compound resazurin, which is reduced to highly fluorescent resorufin in metabolically active cells (excitation/emission peaks at 570/585 nm, respectively). The duration of incubation (72 h) was chosen to allow sufficient time for the antiproliferative effect of doxorubicin on cells to manifest based on reported doubling times 24 and 46 h for MCF7[89] and BT474[90] cells, respectively.

In longer duration/higher dose assays, cells were incubated with aHER2-DOX-MaMAs containing 0.35 μg/mL equivalent of free doxorubicin and magnets below the respective wells for 72 h before a proliferation assay with AlamarBlue. In the wells with magnetic targeting of aHER2-DOX-MaMAs, round 1/2 × 1/4 neodymium magnets (Carolina Biological Supply Company) were mounted below the respective experimental wells at a 5 mm distance from the bottom of the plate using a piece of plastic foam as the spacer and tape for secure mounting. In shorter duration/lower dose assays, cells were incubated with aHER2-DOX-MaMAs at the 0.0875 μg/mL equivalent of free doxorubicin concentration for a total of 2.5 h. Magnets were applied to the respective wells for the first 30 min only. Then, the media were removed from all experimental and control wells and replaced with the fresh media without aHER2-DOX-MaMas. Cells were incubated for another 72 h before a proliferation assay with AlamarBlue. Following the incubation, 20 μL of the AlamarBlue reagent was added to all experimental wells, untreated cells, and the blank media control. Cells were incubated with AlamarBlue for 6 h, and the plates were read in a Synergy H1 fluorometer/plate reader (Biotek) at 560/590 nm excitation/emission, respectively. Fluorescent values from blank media control wells were used

to correct for background fluorescence in experimental wells. STATISTICA 13 (Dell Inc.) was used for statistical analysis (ANOVA) on background-corrected fluorescence values from experimental wells. The type of treatment (untreated control; aHER2-DOX-MaMAs alone; aHER2-DOX-MaMAs + magnet) and plate (to reduce plate-to-plate variability) were used as independent grouping variables. Following the overall ANOVA test and validity assessment, differences between experimental treatments were assessed using the post-hoc Tukey test. Proliferation inhibition values in experimental treatment groups were calculated as % relative to the untreated control (set at 100%) and used for data presentation.

■ ASSOCIATED CONTENT

Ⓢ Supporting Information

The Supporting Information is available free of charge at https://pubs.acs.org/doi/10.1021/acs.bioconjchem.2c00167.

Additional experimental data including characterization of MaMAs, stability testing, EM imaging, and fluorescence image analyses (PDF)

Stacks of cross-sectional images from cryo-EM imaging of MaMAs (Movie S1) (MP4)

Stacks of cross-sectional images from cryo-EM imaging of MaMAs (Movie S2) (MP4)

Stacks of cross-sectional images from cryo-EM imaging of MaMAs (Movie S3) (MP4)

Stacks of cross-sectional images from cryo-EM imaging of MaMAs (Movie S4) (MP4)

■ AUTHOR INFORMATION

Corresponding Author

Konstantin Sokolov − *Department of Imaging Physics, The University of Texas MD Anderson Cancer Center, Houston, Texas 77030, United States; Department of Bioengineering, Rice University, Houston, Texas 77005, United States; Department of Biomedical Engineering, The University of Texas at Austin, Austin, Texas 78712, United States; Present Address: 1881 East Road, Houston, Texas 77054, United States;* ⓞ orcid.org/0000-0002-0198-2005; Email: ksokolov@mdanderson.org

Authors

Chang Soo Kim − *Department of Imaging Physics, The University of Texas MD Anderson Cancer Center, Houston, Texas 77030, United States*

Dmitry Nevozhay − *Department of Imaging Physics, The University of Texas MD Anderson Cancer Center, Houston, Texas 77030, United States*

Rebeca Romero Aburto − *Department of Imaging Physics, The University of Texas MD Anderson Cancer Center, Houston, Texas 77030, United States*

Ashok Pehere − *Department of Imaging Physics, The University of Texas MD Anderson Cancer Center, Houston, Texas 77030, United States*

Lan Pang − *Department of Experimental Therapeutics, The University of Texas MD Anderson Cancer Center, Houston, Texas 77030, United States*

Rebecca Dillard − *Center for Molecular Microscopy, Frederick National Laboratory for Cancer Research, Center for Cancer Research, National Cancer Institute, NIH, Frederick, Maryland 21701, United States*

Ziqiu Wang − *Center for Molecular Microscopy, Frederick National Laboratory for Cancer Research, Center for Cancer Research, National Cancer Institute, NIH, Frederick, Maryland 21701, United States*

Clayton Smith − *Center for Molecular Microscopy, Frederick National Laboratory for Cancer Research, Center for Cancer Research, National Cancer Institute, NIH, Frederick, Maryland 21701, United States*

Kelsey Boitnott Mathieu − *Department of Imaging Physics, The University of Texas MD Anderson Cancer Center, Houston, Texas 77030, United States*

Marie Zhang − *Imagion Biosystems, Inc., San Diego, California 92121, United States*

John D. Hazle − *Department of Imaging Physics, The University of Texas MD Anderson Cancer Center, Houston, Texas 77030, United States*

Robert C. Bast, Jr. − *Department of Experimental Therapeutics, The University of Texas MD Anderson Cancer Center, Houston, Texas 77030, United States*

Complete contact information is available at:
https://pubs.acs.org/10.1021/acs.bioconjchem.2c00167

Author Contributions

[∇]C.S.K., D.N., and R.R.A. contributed equally to this work.

Notes

The authors declare the following competing financial interest(s): M.Z. is an employee of Imagion Biosystems. J.D.H. is a member of the Scientific Advisory Board, Imagion Biosystems.

■ ABBREVIATIONS

DLS, dynamic light scattering; MaMA, magnetic multimicelle aggregate; TEM, transmission electron microscopy; ELISA, enzyme-linked immunosorbent assay; DBCO, dibenzocyclooctyne group; aHER2-MaMAs, magnetic multimicelle aggregate conjugated with anti-HER2 monoclonal antibodies; ICP-MS, inductively coupled plasma mass spectrometry; A647-aHER-MaMAs, magnetic multimicelle aggregate conjugated with anti-HER2 monoclonal antibodies fluorescently labeled with Alexa Fluor 647 dye; aHER2-DOX-MaMAs, magnetic multimicelle aggregate loaded with doxorubicin and conjugated with anti-HER2 monoclonal antibodies

■ REFERENCES

(1) Filipczak, N.; Pan, J.; Yalamarty, S. S. K.; Torchilin, V. P. Recent advancements in liposome technology. *Adv. Drug Delivery Rev.* **2020**, *156*, 4−22.

(2) Ahmed, K. S.; Hussein, S. A.; Ali, A. H.; Korma, S. A.; Lipeng, Q.; Jinghua, C. Liposome: composition, characterisation, preparation, and recent innovation in clinical applications. *J. Drug Target.* **2019**, *27*, 742−761.

(3) Jensen, G. M.; Hodgson, D. F. Opportunities and challenges in commercial pharmaceutical liposome applications. *Adv. Drug Delivery Rev.* **2020**, *154−155*, 2−12.

(4) Al-Jamal, W. T.; Kostarelos, K. Liposomes: from a clinically established drug delivery system to a nanoparticle platform for theranostic nanomedicine. *Acc. Chem. Res.* **2011**, *44*, 1094−1104.

(5) Carter, K. A.; Shao, S.; Hoopes, M. I.; Luo, D.; Ahsan, B.; Grigoryants, V. M.; Song, W.; Huang, H.; Zhang, G.; Pandey, R. K.; et al. Porphyrin-phospholipid liposomes permeabilized by near-infrared light. *Nat. Commun.* **2014**, *5*, No. 3546.

(6) Luo, D.; Carter, K. A.; Razi, A.; Geng, J.; Shao, S.; Giraldo, D.; Sunar, U.; Ortega, J.; Lovell, J. F. Doxorubicin encapsulated in stealth liposomes conferred with light-triggered drug release. *Biomaterials* **2016**, *75*, 193−202.

(7) Klibanov, A. L.; Maruyama, K.; Beckerleg, A. M.; Torchilin, V. P.; Huang, L. Activity of amphipathic poly(ethylene glycol) 5000 to prolong the circulation time of liposomes depends on the liposome size and is unfavorable for immunoliposome binding to target. *Biochim. Biophys. Acta* **1991**, *1062*, 142−148.

(8) Torchilin, V. P.; Klibanov, A. L. Coupling and Labeling of Phospholipids. In *Phospholipids Handbook*, Cevc, G.; Allen, T. M.; Neidleman, S. L., Eds.; Marcel Dekker, Inc.: New York, 1993; pp 293−321.

(9) Xu, F.; Bandara, A.; Akiyama, H.; Eshaghi, B.; Stelter, D.; Keyes, T.; Straub, J. E.; Gummuluru, S.; Reinhard, B. M. Membrane-wrapped nanoparticles probe divergent roles of GM3 and phosphatidylserine in lipid-mediated viral entry pathways. *Proc. Natl. Acad. Sci. U.S.A.* **2018**, *115*, E9041−E9050.

(10) Esparza, K.; Jayawardena, D.; Onyuksel, H. Phospholipid Micelles for Peptide Drug Delivery. *Methods Mol. Biol.* **2019**, *2000*, 43−57.

(11) Gill, K. K.; Kaddoumi, A.; Nazzal, S. PEG-lipid micelles as drug carriers: physiochemical attributes, formulation principles and biological implication. *J. Drug Target.* **2015**, *23*, 222−231.

(12) Mulder, W. J. M.; Strijkers, G. J.; van Tilborg, G. A.; Griffioen, A. W.; Nicolay, K. Lipid-based nanoparticles for contrast-enhanced MRI and molecular imaging. *NMR Biomed.* **2006**, *19*, 142−164.

(13) Barenholz, Y. Doxil(R)–the first FDA-approved nano-drug: lessons learned. *J. Controlled Release* **2012**, *160*, 117−134.

(14) Choi, Y. H.; Han, H. K. Nanomedicines: current status and future perspectives in aspect of drug delivery and pharmacokinetics. *J. Pharm. Investig.* **2018**, *48*, 43−60.

(15) Marchal, S.; El Hor, A.; Millard, M.; Gillon, V.; Bezdetnaya, L. Anticancer Drug Delivery: An Update on Clinically Applied Nanotherapeutics. *Drugs* **2015**, *75*, 1601−1611.

(16) Belfiore, L.; Saunders, D. N.; Ranson, M.; Thurecht, K. J.; Storm, G.; Vine, K. L. Towards clinical translation of ligand-functionalized liposomes in targeted cancer therapy: Challenges and opportunities. *J. Controlled Release* **2018**, *277*, 1−13.

(17) Wicki, A.; Witzigmann, D.; Balasubramanian, V.; Huwyler, J. Nanomedicine in cancer therapy: challenges, opportunities, and clinical applications. *J. Controlled Release* **2015**, *200*, 138−157.

(18) Beilvert, A.; Cormode, D. P.; Chaubet, F.; Briley-Saebo, K. C.; Mani, V.; Mulder, W. J.; Vucic, E.; Toussaint, J. F.; Letourneur, D.; Fayad, Z. A. Tyrosine polyethylene glycol (PEG)-micelle magnetic resonance contrast agent for the detection of lipid rich areas in atherosclerotic plaque. *Magn. Reson. Med.* **2009**, *62*, 1195−1201.

(19) den Adel, B.; van der Graaf, L. M.; Que, I.; Strijkers, G. J.; Lowik, C. W.; Poelmann, R. E.; van der Weerd, L. Contrast enhancement by lipid-based MRI contrast agents in mouse

atherosclerotic plaques; a longitudinal study. *Contrast Media Mol. Imaging* **2013**, *8*, 63−71.

(20) Mulder, W. J. M.; Strijkers, G. J.; Briley-Saboe, K. C.; Frias, J. C.; Aguinaldo, J. G.; Vucic, E.; Amirbekian, V.; Tang, C.; Chin, P. T.; Nicolay, K.; Fayad, Z. A. Molecular imaging of macrophages in atherosclerotic plaques using bimodal PEG-micelles. *Magn. Reson. Med.* **2007**, *58*, 1164−1170.

(21) Krishnadas, A.; Rubinstein, I.; Onyuksel, H. Sterically stabilized phospholipid mixed micelles: in vitro evaluation as a novel carrier for water-insoluble drugs. *Pharm. Res.* **2003**, *20*, 297−302.

(22) Tang, N.; Du, G.; Wang, N.; Liu, C.; Hang, H.; Liang, W. Improving penetration in tumors with nanoassemblies of phospholipids and doxorubicin. *J. Natl. Cancer Inst.* **2007**, *99*, 1004−1015.

(23) Koo, O. M. Y.; Rubinstein, I.; Onyuksel, H. Actively targeted low-dose camptothecin as a safe, long-acting, disease-modifying nanomedicine for rheumatoid arthritis. *Pharm. Res.* **2011**, *28*, 776−787.

(24) Mu, L.; Elbayoumi, T. A.; Torchilin, V. P. Mixed micelles made of poly(ethylene glycol)-phosphatidylethanolamine conjugate and d-alpha-tocopheryl polyethylene glycol 1000 succinate as pharmaceutical nanocarriers for camptothecin. *Int. J. Pharm.* **2005**, *306*, 142−149.

(25) Önyüksel, H.; Ikezaki, H.; Patel, M.; Gao, X. P.; Rubinstein, I. A novel formulation of VIP in sterically stabilized micelles amplifies vasodilation in vivo. *Pharm. Res.* **1999**, *16*, 155−160.

(26) Soetaert, F.; Korangath, P.; Serantes, D.; Fiering, S.; Ivkov, R. Cancer therapy with iron oxide nanoparticles: Agents of thermal and immune therapies. *Adv. Drug Delivery Rev.* **2020**, *163−164*, 65−83.

(27) Bhandari, S.; Pereira, D. I. A.; Chappell, H. F.; Drakesmith, H. Intravenous Irons: From Basic Science to Clinical Practice. *Pharmaceuticals* **2018**, *11*, No. 82.

(28) Auerbach, M.; Deloughery, T. Single-dose intravenous iron for iron deficiency: a new paradigm. *Hematology* **2016**, *2016*, 57−66.

(29) Wang, Y. X. Current status of superparamagnetic iron oxide contrast agents for liver magnetic resonance imaging. *World J. Gastroenterol.* **2015**, *21*, 13400−13402.

(30) Thiesen, B.; Jordan, A. Clinical applications of magnetic nanoparticles for hyperthermia. *Int. J. Hyperthermia* **2008**, *24*, 467−474.

(31) Maier-Hauff, K.; Ulrich, F.; Nestler, D.; Niehoff, H.; Wust, P.; Thiesen, B.; Orawa, H.; Budach, V.; Jordan, A. Efficacy and safety of intratumoral thermotherapy using magnetic iron-oxide nanoparticles combined with external beam radiotherapy on patients with recurrent glioblastoma multiforme. *J. Neurooncol.* **2011**, *103*, 317−324.

(32) Oldenburg, A. L.; Toublan, F.; Suslick, K.; Wei, A.; Boppart, S. Magnetomotive contrast for in vivo optical coherence tomography. *Opt. Express* **2005**, *13*, 6597−6614.

(33) Aaron, J. S.; Oh, J.; Larson, T. A.; Kumar, S.; Milner, T. E.; Sokolov, K. V. Increased optical contrast in imaging of epidermal growth factor receptor using magnetically actuated hybrid gold/iron oxide nanoparticles. *Opt. Express* **2006**, *14*, 12930−12943.

(34) Mehrmohammadi, M.; Shin, T. H.; Qu, M.; Kruizinga, P.; Truby, R. L.; Lee, J. H.; Cheon, J.; Emelianov, S. Y. In vivo pulsed magneto-motive ultrasound imaging using high-performance magnetoactive contrast nanoagents. *Nanoscale* **2013**, *5*, 11179−11186.

(35) Qu, M.; Mallidi, S.; Mehrmohammadi, M.; Truby, R.; Homan, K.; Joshi, P.; Chen, Y. S.; Sokolov, K.; Emelianov, S. Magneto-photoacoustic imaging. *Biomed. Opt. Express* **2011**, *2*, 385−396.

(36) Snider, E. J.; Kubelick, K. P.; Tweed, K.; Kim, R. K.; Li, Y.; Gao, K.; Read, A. T.; Emelianov, S.; Ethier, C. R. Improving Stem Cell Delivery to the Trabecular Meshwork Using Magnetic Nanoparticles. *Sci. Rep.* **2018**, *8*, No. 12251.

(37) Kamei, G.; Kobayashi, T.; Ohkawa, S.; Kongcharoensombat, W.; Adachi, N.; Takazawa, K.; Shibuya, H.; Deie, M.; Hattori, K.; Goldberg, J. L.; Ochi, M. Articular cartilage repair with magnetic mesenchymal stem cells. *Am. J. Sports Med.* **2013**, *41*, 1255−1264.

(38) Vanecek, V.; Zablotskii, V.; Forostyak, S.; Ruzicka, J.; Herynek, V.; Babic, M.; Jendelova, P.; Kubinova, S.; Dejneka, A.; Sykova, E. Highly efficient magnetic targeting of mesenchymal stem cells in spinal cord injury. *Int. J. Nanomed.* **2012**, *7*, 3719−3730.

(39) Rohiwal, S. S.; Dvorakova, N.; Klima, J.; Vaskovicova, M.; Senigl, F.; Slouf, M.; Pavlova, E.; Stepanek, P.; Babuka, D.; Benes, H.; et al. Polyethylenimine based magnetic nanoparticles mediated non-viral CRISPR/Cas9 system for genome editing. *Sci. Rep.* **2020**, *10*, No. 4619.

(40) Hryhorowicz, M.; Grzeskowiak, B.; Mazurkiewicz, N.; Sledzinski, P.; Lipinski, D.; Slomski, R. Improved Delivery of CRISPR/Cas9 System Using Magnetic Nanoparticles into Porcine Fibroblast. *Mol. Biotechnol.* **2019**, *61*, 173−180.

(41) Zhu, H.; Zhang, L.; Tong, S.; Lee, C. M.; Deshmukh, H.; Bao, G. Spatial control of in vivo CRISPR-Cas9 genome editing via nanomagnets. *Nat. Biomed. Eng.* **2019**, *3*, 126−136.

(42) Mangarova, D. B.; Brangsch, J.; Mohtashamdolatshahi, A.; Kosch, O.; Paysen, H.; Wiekhorst, F.; Klopfleisch, R.; Buchholz, R.; Karst, U.; Taupitz, M.; et al. Ex vivo magnetic particle imaging of vascular inflammation in abdominal aortic aneurysm in a murine model. *Sci. Rep.* **2020**, *10*, No. 12410.

(43) Liang, X.; Wang, K.; Du, J.; Tian, J.; Zhang, H. The first visualization of chemotherapy-induced tumor apoptosis via magnetic particle imaging in a mouse model. *Phys. Med. Biol.* **2020**, *65*, No. 195004.

(44) Thrower, S. L.; Kandala, S. K.; Fuentes, D.; Stefan, W.; Sowko, N.; Huang, M.; Mathieu, K.; Hazle, J. D. A compressed sensing approach to immobilized nanoparticle localization for superparamagnetic relaxometry. *Phys. Med. Biol.* **2019**, *64*, No. 194001.

(45) Margolis, L. B.; Namiot, V. A.; Kljukin, L. M. Magnetoliposomes: another principle of cell sorting. *Biochim. Biophys. Acta* **1983**, *735*, 193−195.

(46) De Cuyper, M.; Joniau, M. Magnetoliposomes. Formation and structural characterization. *Eur. Biophys. J.* **1988**, *15*, 311−319.

(47) Starmans, L. W. E.; Moonen, R. P.; Aussems-Custers, E.; Daemen, M. J.; Strijkers, G. J.; Nicolay, K.; Grull, H. Evaluation of iron oxide nanoparticle micelles for magnetic particle imaging (MPI) of thrombosis. *PLoS One* **2015**, *10*, No. e0119257.

(48) Tai, L. A.; Tsai, P. J.; Wang, Y. C.; Wang, Y. J.; Lo, L. W.; Yang, C. S. Thermosensitive liposomes entrapping iron oxide nanoparticles for controllable drug release. *Nanotechnology* **2009**, *20*, No. 135101.

(49) Chen, Y.; Bose, A.; Bothun, G. D. Controlled release from bilayer-decorated magnetoliposomes via electromagnetic heating. *ACS Nano* **2010**, *4*, 3215−3221.

(50) Gao, W.; Wei, S.; Li, Z.; Li, L.; Zhang, X.; Li, C.; Gao, D. Nano magnetic liposomes-encapsulated parthenolide and glucose oxidase for ultra-efficient synergistic antitumor therapy. *Nanotechnology* **2020**, *31*, No. 355104.

(51) Ye, H.; Tong, J.; Liu, J.; Lin, W.; Zhang, C.; Chen, K.; Zhao, J.; Zhu, W. Combination of gemcitabine-containing magnetoliposome and oxaliplatin-containing magnetoliposome in breast cancer treatment: A possible mechanism with potential for clinical application. *Oncotarget* **2016**, *7*, 43762−43778.

(52) Mikhaylov, G.; Mikac, U.; Magaeva, A. A.; Itin, V. I.; Naiden, E. P.; Psakhye, I.; Babes, L.; Reinheckel, T.; Peters, C.; Zeiser, R.; et al. Ferri-liposomes as an MRI-visible drug-delivery system for targeting tumours and their microenvironment. *Nat. Nanotechnol.* **2011**, *6*, 594−602.

(53) Ribeiro, R. S. G.; Gysemans, C.; da Cunha, J.; Manshian, B. B.; Jirak, D.; Kriz, J.; Gallo, J.; Banobre-Lopez, M.; Struys, T.; De Cuyper, M.; et al. Magnetoliposomes as Contrast Agents for Longitudinal in vivo Assessment of Transplanted Pancreatic Islets in a Diabetic Rat Model. *Sci. Rep.* **2018**, *8*, No. 11487.

(54) Bulte, J. W. M.; Ma, L. D.; Magin, R. L.; Kamman, R. L.; Hulstaert, C. E.; Go, K. G.; The, T. H.; De Leij, L. Selective MR imaging of labeled human peripheral blood mononuclear cells by liposome mediated incorporation of dextran-magnetite particles. *Magn. Reson. Med.* **1993**, *29*, 32−37.

(55) Bulte, J. W. M.; Cuyper, Md.; Despres, D.; Frank, J. A. Preparation, relaxometry, and biokinetics of PEGylated magnetoliposomes as MR contrast agent. *J. Magn. Magn. Mater.* **1999**, *194*, 204−209.

(56) Bulte, J. W. M.; de Cuyper, M.; Despres, D.; Frank, J. A. Short- vs. long-circulating magnetoliposomes as bone marrow-seeking MR contrast agents. *J. Magn. Reson. Imaging* **1999**, *9*, 329−335.

(57) Xu, H. L.; Yang, J. J.; ZhuGe, D. L.; Lin, M. T.; Zhu, Q. Y.; Jin, B. H.; Tong, M. Q.; Shen, B. X.; Xiao, J.; Zhao, Y. Z. Glioma-Targeted Delivery of a Theranostic Liposome Integrated with Quantum Dots, Superparamagnetic Iron Oxide, and Cilengitide for Dual-Imaging Guiding Cancer Surgery. *Adv. Healthcare Mater.* **2018**, *7*, No. 1701130.

(58) Grippin, A. J.; Wummer, B.; Wildes, T.; Dyson, K.; Trivedi, V.; Yang, C.; Sebastian, M.; Mendez-Gomez, H. R.; Padala, S.; Grubb, M.; et al. Dendritic Cell-Activating Magnetic Nanoparticles Enable Early Prediction of Antitumor Response with Magnetic Resonance Imaging. *ACS Nano* **2019**, *13*, 13884−13898.

(59) Fattahi, H.; Laurent, S.; Liu, F.; Arsalani, N.; Vander Elst, L.; Muller, R. N. Magnetoliposomes as multimodal contrast agents for molecular imaging and cancer nanotheragnostics. *Nanomedicine* **2011**, *6*, 529−544.

(60) Sawant, R. R.; Torchilin, V. P. Liposomes as 'smart' pharmaceutical nanocarriers. *Soft Matter* **2010**, *6*, 4026−4044.

(61) Zhang, L. L.; Tong, S.; Zhang, Q. B.; Bao, G. Lipid-Encapsulated Fe3O4 Nanoparticles for Multimodal Magnetic Resonance/Fluorescence Imaging. *ACS Appl. Nano Mater.* **2020**, *3*, 6785−6797.

(62) He, J.; Huang, X.; Li, Y. C.; Liu, Y.; Babu, T.; Aronova, M. A.; Wang, S.; Lu, Z.; Chen, X.; Nie, Z. Self-assembly of amphiphilic plasmonic micelle-like nanoparticles in selective solvents. *J. Am. Chem. Soc.* **2013**, *135*, 7974−7984.

(63) Qiu, F.; Wang, D.; Zhu, Q.; Zhu, L.; Tong, G.; Lu, Y.; Yan, D.; Zhu, X. Real-time monitoring of anticancer drug release with highly fluorescent star-conjugated copolymer as a drug carrier. *Biomacromolecules* **2014**, *15*, 1355−1364.

(64) Hong, H. Y.; Mai, Y. Y.; Zhou, Y. F.; Yan, D. Y.; Cui, J. Self-assembly of large multimolecular micelles from hyperbranched star copolymers. *Macromol. Rapid Commun.* **2007**, *28*, 591−596.

(65) Qi, M. W.; Zhou, Y. F. Multimicelle aggregate mechanism for spherical multimolecular micelles: from theories, characteristics and properties to applications. *Mater. Chem. Front.* **2019**, *3*, 1994−2009.

(66) Tong, S.; Hou, S.; Zheng, Z.; Zhou, J.; Bao, G. Coating optimization of superparamagnetic iron oxide nanoparticles for high T2 relaxivity. *Nano Lett.* **2010**, *10*, 4607−4613.

(67) Tong, S.; Hou, S.; Ren, B.; Zheng, Z.; Bao, G. Self-assembly of phospholipid-PEG coating on nanoparticles through dual solvent exchange. *Nano Lett.* **2011**, *11*, 3720−3726.

(68) Hemben, A.; Chianella, I.; Leighton, G. J. T. Surface Engineered Iron Oxide Nanoparticles Generated by Inert Gas Condensation for Biomedical Applications. *Bioengineering* **2021**, *8*, No. 38.

(69) Liu, C. H.; Nevozhay, D.; Schill, A.; Singh, M.; Das, S.; Nair, A.; Han, Z.; Aglyamov, S.; Larin, K. V.; Sokolov, K. V. Nanobomb optical coherence elastography. *Opt. Lett.* **2018**, *43*, 2006−2009.

(70) Liu, C. H.; Nevozhay, D.; Zhang, H.; Das, S.; Schill, A.; Singh, M.; Aglyamov, S.; Sokolov, K. V.; Larin, K. V. Longitudinal elastic wave imaging using nanobomb optical coherence elastography. *Opt. Lett.* **2019**, *44*, 3162−3165.

(71) Nevozhay, D.; Weiger, M.; Friedl, P.; Sokolov, K. V. Spatiotemporally controlled nano-sized third harmonic generation agents. *Biomed. Opt. Express* **2019**, *10*, 3301−3316.

(72) Boerner, P.; Nevozhay, D.; Hatamimoslehabadi, M.; Chawla, H. S.; Zvietcovich, F.; Aglyamov, S.; Larin, K. V.; Sokolov, K. V. Repetitive optical coherence elastography measurements with blinking nanobombs. *Biomed. Opt. Express* **2020**, *11*, 6659−6673.

(73) Gabizon, A.; Shmeeda, H.; Barenholz, Y. Pharmacokinetics of pegylated liposomal Doxorubicin: review of animal and human studies. *Clin. Pharmacokinet.* **2003**, *42*, 419−436.

(74) Bulbake, U.; Doppalapudi, S.; Kommineni, N.; Khan, W. Liposomal Formulations in Clinical Use: An Updated Review. *Pharmaceutics* **2017**, *9*, No. 12.

(75) Chang, H. I.; Yeh, M. K. Clinical development of liposome-based drugs: formulation, characterization, and therapeutic efficacy. *Int. J. Nanomed.* **2012**, *7*, 49−60.

(76) Kumar, S.; Aaron, J.; Sokolov, K. Directional conjugation of antibodies to nanoparticles for synthesis of multiplexed optical contrast agents with both delivery and targeting moieties. *Nat. Protoc.* **2008**, *3*, 314−320.

(77) Karver, M. R.; Weissleder, R.; Hilderbrand, S. A. Bioorthogonal reaction pairs enable simultaneous, selective, multi-target imaging. *Angew. Chem., Int. Ed.* **2012**, *51*, 920−922.

(78) Ramil, C. P.; Lin, Q. Bioorthogonal chemistry: strategies and recent developments. *Chem. Commun.* **2013**, *49*, 11007−11022.

(79) Boyce, M.; Bertozzi, C. R. Bringing chemistry to life. *Nat. Methods* **2011**, *8*, 638−642.

(80) Kolb, H. C.; Finn, M. G.; Sharpless, K. B. Click Chemistry: Diverse Chemical Function from a Few Good Reactions. *Angew. Chem., Int. Ed.* **2001**, *40*, 2004−2021.

(81) N'Guyen, T. T. T.; Duong, H. T.; Basuki, J.; Montembault, V.; Pascual, S.; Guibert, C.; Fresnais, J.; Boyer, C.; Whittaker, M. R.; Davis, T. P.; et al. Functional iron oxide magnetic nanoparticles with hyperthermia-induced drug release ability by using a combination of orthogonal click reactions. *Angew. Chem., Int. Ed.* **2013**, *52*, 14152−14156.

(82) Chen, Y.; Xianyu, Y.; Wu, J.; Yin, B.; Jiang, X. Click Chemistry-Mediated Nanosensors for Biochemical Assays. *Theranostics* **2016**, *6*, 969−985.

(83) Klibanov, A. L.; Maruyama, K.; Torchilin, V. P.; Huang, L. Amphipathic polyethyleneglycols effectively prolong the circulation time of liposomes. *FEBS Lett.* **1990**, *268*, 235−237.

(84) Gabizon, A.; Catane, R.; Uziely, B.; Kaufman, B.; Safra, T.; Cohen, R.; Martin, F.; Huang, A.; Barenholz, Y. Prolonged circulation time and enhanced accumulation in malignant exudates of doxorubicin encapsulated in polyethylene-glycol coated liposomes. *Cancer Res.* **1994**, *54*, 987−992.

(85) Dadashzadeh, E. R.; Hobson, M.; Henry Bryant, L., Jr.; Dean, D. D.; Frank, J. A. Rapid spectrophotometric technique for quantifying iron in cells labeled with superparamagnetic iron oxide nanoparticles: potential translation to the clinic. *Contrast Media Mol. Imaging* **2013**, *8*, 50−56.

(86) Kauffman, M. K.; Kauffman, M. E.; Zhu, H.; Jia, Z.; Li, Y. R. Fluorescence-Based Assays for Measuring Doxorubicin in Biological Systems. *React. Oxygen Species* **2016**, *2*, 432−439.

(87) Kremer, J. R.; Mastronarde, D. N.; McIntosh, J. R. Computer visualization of three-dimensional image data using IMOD. *J. Struct. Biol.* **1996**, *116*, 71−76.

(88) Kumar, P.; Nagarajan, A.; Uchil, P. D. Analysis of Cell Viability by the alamarBlue Assay. *Cold Spring Harb. Protoc.* **2018**, *2018*, No. pdb.prot095489.

(89) Sutherland, R. L.; Hall, R. E.; Taylor, I. W. Cell proliferation kinetics of MCF-7 human mammary carcinoma cells in culture and effects of tamoxifen on exponentially growing and plateau-phase cells. *Cancer Res.* **1983**, *43*, 3998−4006.

(90) Strauch, M.; Ludke, A.; Munch, D.; Laudes, T.; Galizia, C. G.; Martinelli, E.; Lavra, L.; Paolesse, R.; Ulivieri, A.; Catini, A.; et al. More than apples and oranges–detecting cancer with a fruit fly's antenna. *Sci. Rep.* **2014**, *4*, No. 3576.